



OPEN

## Optomechanical crystals for spatial sensing of submicron sized particles

D. Navarro-Urrios<sup>1,2</sup>, E. Kang<sup>3</sup>, P. Xiao<sup>2</sup>, M. F. Colombano<sup>1,2</sup>, G. Arregui<sup>2</sup>, B. Graczykowski<sup>3,4</sup>, N. E. Capuj<sup>5,6</sup>, M. Sledzinska<sup>2</sup>, C. M. Sotomayor-Torres<sup>2,7</sup> & G. Fytas<sup>3</sup>

Optomechanical crystal cavities (OMC) have rich perspectives for detecting and indirectly analysing biological particles, such as proteins, bacteria and viruses. In this work we demonstrate the working principle of OMCs operating under ambient conditions as a sensor of submicrometer particles by optically monitoring the frequency shift of thermally activated mechanical modes. The resonator has been specifically designed so that the cavity region supports a particular family of low modal-volume mechanical modes, commonly known as -pinch modes-. These involve the oscillation of only a couple of adjacent cavity cells that are relatively insensitive to perturbations in other parts of the resonator. The eigenfrequency of these modes decreases as the deformation is localized closer to the centre of the resonator. Thus, by identifying specific modes that undergo a frequency shift that amply exceeds the mechanical linewidth, it is possible to infer if there are particles deposited on the resonator, how many are there and their approximate position within the cavity region. OMCs have rich perspectives for detecting and indirectly analysing biological particles, such as proteins, viruses and bacteria.

In the last decade photonic crystals (PhCs) have been used as optical sensing platform, in particular for label-free biosensing<sup>1,2</sup>. PhCs cavities strongly confine light in ultra-low volumes, enabling the detection of chemical species down to nanometric dimensions when placed in close proximity to the cavity region by monitoring the spectral shift of an optical resonance<sup>3</sup>. Alternatively, sensors based on nano-electro-mechanical system (NEMS) can be extremely sensitive as mass and/or force sensors based on the frequency shift of the supported mechanical modes and/or variations of their quality factors<sup>4</sup>. Indeed, they can achieve mass resolution in the nanogram scale and resolve forces as small as 10 pN even when operating in a fluid environment<sup>5</sup>. Both sorts of devices, if combined with advanced chemical surface functionalization techniques and the integration in microfluidic systems<sup>6</sup>, pave the way towards ultra-compact lab-on-chip platforms with very high performance and real time monitoring<sup>7,8</sup>.

More recently, cavity optomechanical systems<sup>9</sup> have also been proposed as successful sensing platforms since they exhibit similar characteristics to those of NEMS while adding the possibility of optically transducing the mechanical motion even in liquid environments<sup>10</sup>. Mechanical modes can be thermally activated by Langevin forces or, by exploiting radiation pressure forces, driven to a regime of coherent high amplitude oscillations<sup>11</sup>. Indeed, in the latter regime, recent experiments have elegantly demonstrated an enhanced sensing resolution down to a single molecule, achieved by monitoring the change of the mechanical spring constant as the optical detuning between the laser and the resonance is modified<sup>12</sup>.

A particularly suited class of cavity optomechanical system for sensing applications are optomechanical crystal cavities (OMC's), nanostructured materials which simultaneously behave as photonic and phononic crystal cavities<sup>13</sup>. They can provide a combination of the sensing characteristics of PhCs and NEMS and extend further the sensing capabilities of these systems by exploiting optomechanical coupling effects, which are engineered by structural design<sup>14-16</sup>. In this work we present a novel OMC-based sensing device that addresses the issue of counting and spatially localizing submicrometric analytes. In fact, this is a pervasive issue that often compromises the analysis of the registered data. For instance, when dealing with standard NEMS sensors such as cantilevers or

<sup>1</sup>MIND-IN2UB, Departament d'Enginyeria Electrònica i Biomèdica, Facultat de Física, Universitat de Barcelona, Martí i Franquès 1, 08028 Barcelona, Spain. <sup>2</sup>Catalan Institute of Nanoscience and Nanotechnology (ICN2), CSIC and BIST, Campus UAB, Bellaterra, 08193 Barcelona, Spain. <sup>3</sup>Max Planck Institute for Polymer Research, Ackermannweg 10, 55128 Mainz, Germany. <sup>4</sup>Faculty of Physics, Adam Mickiewicz University, Uniwersytetu Poznańskiego 2, 61614 Poznań, Poland. <sup>5</sup>Depto. Física, Universidad de La Laguna, 38200 San Cristóbal de La Laguna, Spain. <sup>6</sup>Instituto Universitario de Materiales y Nanotecnología, Universidad de La Laguna, 38071 Santa Cruz de Tenerife, Spain. <sup>7</sup>Catalan Institute for Research and Advances Studies ICREA, 08010 Barcelona, Spain. ✉email: dnavarro@ub.edu; fytas@mpip-mainz.mpg.de

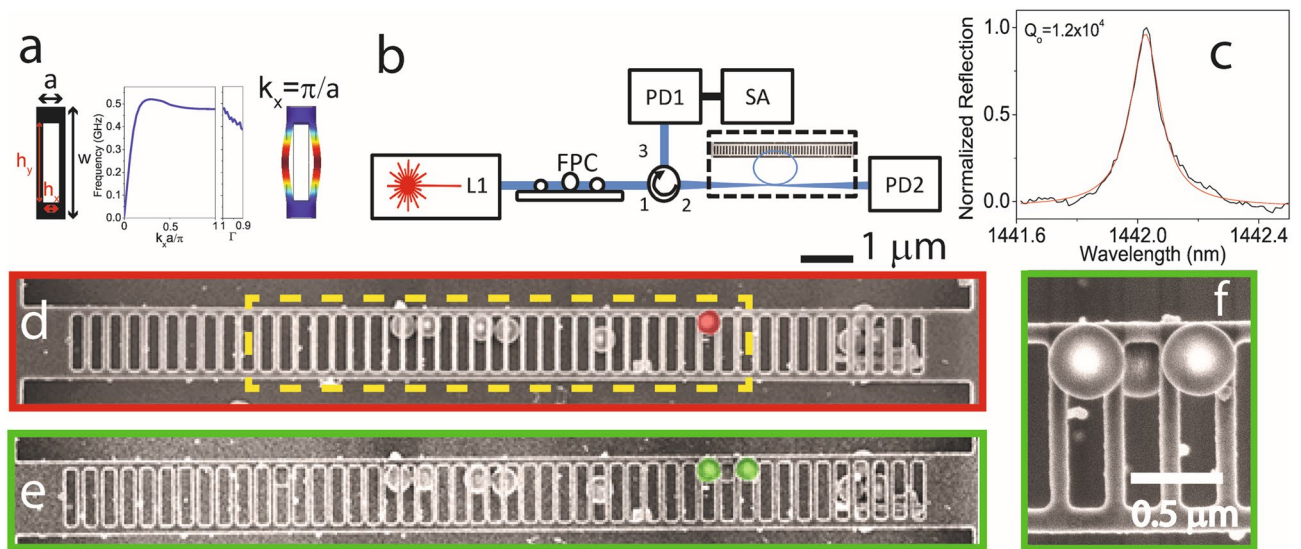


**Figure 1.** Optomechanical crystal geometry and experimental setup. **(a)** Left. Sketch of the unit cell of the OMC. The nominal geometrical parameters are  $a = 362$  nm,  $w = 1396$  nm,  $h_y = 992$  nm,  $h_x = 190$  nm and thickness = 250 nm. Centre. Band diagram of the pinch mechanical band and dependence of the X-point band edge energy on the reduction factor. Right. Deformation profile of the pinch mode at the X-point calculated with a FEM solver. The simulations have been performed by importing single mirror cells of the fabricated geometry and applying Floquet periodic conditions. **(b)** Experimental setup used for the optomechanical characterization of the fabricated OMCs. **(c)** Reflection spectra around the first optical resonance of the OMC. **(d,e)** SEM micrographs of the characterized OMCs with one and two submicrometer particles on top and have been highlighted in red and green, respectively. The cavity region is delineated by a dashed yellow box in **(d)**. **(f)** Zoom of the region of the OMC holding the particles. The diameter of the particles is  $495 \pm 16$  nm.

strings over which one or several analytes are positioned, their effect on the mechanical mode of the resonator significantly depends on their specific location<sup>5</sup>.

Here the proposed design exploits low modal-volume mechanical modes –pinch modes– that involve the oscillation of a few adjacent crossbars of the cavity cells and are relatively insensitive to perturbations in other parts of the resonator. We show that, in most cases, the mechanical modes are spatially modified in a way that the analyte blocks the affected crossbars due to its additional mass. Thus, the observed frequency shift is independent of the elastic properties of the analyte or its adhesion force to the OMC. In order to extract more information about the analyte, we discuss the possibility of bringing together its natural frequencies to that of the affected pinch mode so that both modes hybridize. We also consider the emergence of new mechanical modes involving the collective oscillation of the affected crossbars and the analyte, the frequency of which depends mostly on the analyte mass.

### Description of the geometries and experimental setup

The fabricated structures are 1-dimensional silicon OMCs based on a unit cell consisting of a crystalline silicon rectangular block of lattice constant  $a$  with a rectangular hole. In this work we focus on the lowest energy frequency even-even mechanical band that is commonly known as ‘pinch’ mode band, which, for the present fabricated structure, lies below 0.6 GHz<sup>13,17</sup>. The band diagram has been computed with a finite elements method (FEM) solver both using an imported cell of the fabricated structure and the nominal cell (central panel of Fig. 1a and Supplementary Information, respectively). The pinch mode is a localized, in-plane mechanical vibration and its deformation profile for a wave number  $k_x = \pi/a$  in the axial direction of the OMC, i.e., at the X-point, is illustrated in Fig. 1a.

The cavity region is highlighted in Fig. 1d with a dashed yellow box and consists of an odd number of holes with the spacing between them reduced quadratically from the nominal lattice constant at the beam perimeter ( $a$ ) to  $\Gamma a$  for the cell in the centre of the OMC ( $\Gamma < 1$ ). On both sides of the OMC the nominal cell is repeated 10 times, thus acting as an effective mirror for optical and mechanical cavity modes. Optical modes are drawn up in energy from the X-point of a TE-like band, which is placed at about 170 THz. In this sense, the depth of the cavity region has been engineered so that it supports optical modes within the spectral range of our light sources, i.e., between 180 and 210 THz. Given that the pinch mechanical modes are drawn from a band edge at the X-point, each crossbar vibrates 180° out of phase with respect to its nearest neighbors. Consequently, vibration of neighboring cells add up in anti-phase to the overall optomechanical coupling. If the cells composing the cavity region are sufficiently different, a pinch cavity mode is localized just in one or two cells, otherwise it involves the deformation of several cells. In terms of the sensor design, this implies that the cavity region cannot be distributed over an arbitrary large number of cells, since the spatial resolution would be lost at the expense of increasing the sensing area. Thus, a compromise has been found considering the number of cells, pinch modes spatial localization and spectral resolution ( $> 1$ –2 MHz, the experimental mechanical linewidth). The

cavity region was therefore distributed over 27 cells and the maximum reduction of the pitch in the centre of the OMC was  $\Gamma = 0.9$ . The total number of cells composing the OMC is 47 and the sensing area is about  $12 \mu\text{m}^2$  (see Fig. 1d). As illustrated in Fig. 1a by plotting the band edge at the X-point as a function of  $\Gamma$  the confinement potential pushes the pinch band to lower frequencies. This implies that the pinch modes within the cavity region have eigenfrequencies ( $\Omega_{m,o}$ ) of decreasing values as the modes are localized in cells closer to the centre. More details concerning the nominal design and the fabrication of the OMCs can be found in the Supplementary Information (Sections S1 to S3).

Submicrometer silica particles (diameter  $d = 495 \pm 16 \text{ nm}$ ) were dispersed in ethanol up to a concentration of 38 mg/L. After ethanol evaporation, several particles were deposited on the OMCs. Other particles remained underneath the OMCs sitting on the silicon substrate, which lays  $2 \mu\text{m}$  below the OMC, since the last ethanol volume prior to evaporation lies under the OMC. We ensured that these particles were not in contact with the OMC by SEM inspection in a tilted configuration and therefore do not have any effect on the measurements described in this work (see SI, Section S8).

The experiments were made in a standard set-up to characterize optical and mechanical properties of OMCs (Fig. 1). A tuneable infrared laser (L1) covering the spectral range 1440–1640 nm was connected to a tapered fibre in the shape of a microloop<sup>18</sup>. The polarization state of the light entering the tapered region was set with a polarization controller (FPC). The fibre was brought into contact with the etched frame, while the thinnest part of the fibre rests above the central region of the OM crystal. The long tail of the evanescent field, which is several hundreds of nanometers, and the low spatial resolution ( $\sim 5 \mu\text{m}^2$ ) of the tapered fibre allowed the local excitation of resonant optical modes of the OMC (Fig. 1b).

The OMC is a bi-directional photonic cavity, hence it can optically couple to both forward and backward propagating fibre modes. By using a fibre circulator it is possible to collect both the reflected and transmitted signals, which are detected by InGaAs fast photoreceivers PD1 and PD2, respectively. Figure 1c shows a normalized reflected spectrum of the OMC under study around the highest energy optical resonance within the spectral range of the tuneable laser. The optical quality factor of this particular mode is on the order of  $10^4$ , while the coupled power fraction, i.e., the amount of coupled optical power as referred to the incident one, exceeds 90%. To check for the presence of a radiofrequency (RF) modulation of the reflected signal we connect the output of PD1 to the  $50 \Omega$  input impedance of a signal analyser (SA) with a bandwidth of 13.5 GHz. All the measurements were performed in an anti-vibration cage at ambient conditions. The experimental approach requires the optical transduction of the mechanical spectrum of a specific OMC when there is one particle (Fig. 1d) and two particles (Fig. 1e,f) on the OMC. Both are compared to the reference mechanical spectrum of the OMC without particles.

The followed procedure to position the particles was first to deposit two particles on the OMC, which were positioned only two cells away from each other on the outer cells of the cavity region after the ethanol evaporated (Fig. 1e). We then proceeded to remove the particle placed further from the centre (Fig. 1d) and finally the remaining one using the tip of a tapered fibre. It is worth noting that the optical spectra did not suffer significant changes when depositing the particles. Indeed, because of the rather low refractive index of the particles in comparison with that of silicon and the small overlap between the particles and the optical mode, the latter appeared at roughly the same spectral position with similar quality factors as that of Fig. 1c during the whole experiment.

## FEM simulations of the fabricated OMC

To model the fabricated OMC and account for the differences from the nominal design, the in-plane geometry was imported from the SEM micrographs into a FEM solver, where the thickness is that of the top Si layer of the SOI wafer. This procedure ensures a reasonably good agreement between the measured optical and mechanical modes and those extracted from simulations. We have also considered the case of including a spherical  $\text{SiO}_2$  particle positioned on one of the crossbars of the OMC, aiming to resemble the situation reported in the SEM micrograph of Fig. 1d.

Figure 2b shows the computed spectral dependence of the single-particle OM coupling rate ( $g_o/2\pi$ ) without the particle taking into account photo-elastic and moving-boundary contributions (see SI, Sections S2 and S3)<sup>18</sup>. The optical mode used for these calculations (see Fig. 2a) appears at around 200 THz and it was checked that it is not meaningfully affected by the presence of the particle (not shown), which is consistent with the experiment observation. We measure a sizeable reduction of the expected values of  $\Omega_{m,o}$  with respect to the nominal design (details in SI, Section S3) associated to an effective increase of  $h_x$  of the fabricated geometries. In order to mimic the experimental RF spectrum, we have represented each mode by a Lorentzian line shape and added up the contributions of all modes. The inspection of the spatial profile of the mechanical modes providing large  $g_o$  supports their association to pinch-like modes, also confirming that  $\Omega_{m,o}$  decreases as the modes become localized closer to the centre of the OMC (details in SI, Section S3). Notably, not all pinch modes display large coupling  $g_o$  values, so these modes would be eventually hidden below the noise level of the experiment. The mass and modal volume of such modes are on the order of 0.1 pg and  $0.1 \mu\text{m}^3$ , respectively.

Figure 2c reports the frequency shift of the mechanical modes ( $\Delta\Omega$ ) with respect to the original eigenfrequency  $\Omega_{m,o}$  when the particle is introduced. We observe a significant shift towards higher frequencies exceeding 0.3% whenever the original mode involves the crossbar with the particle. As expected, the modes affected to a greater extent appear in the high frequency range, given that the particle is placed almost at the boundary of the cavity region and higher frequency modes tend to localize away from the center (details in SI, Section S3). This is illustrated for the mode highlighted with the green dashed box, which displays both large coupling  $g_o$  and  $\Delta\Omega$  values. The deformation profiles of that particular mode with and without the particle are displayed in Fig. 2d (bottom and top panels, respectively). Since the presence of the particle substantially increases the overall mass of the crossbar, the original mode accommodates to a new spatial configuration in which that crossbar remains fixed. We have also modified the Young modulus and density of the particle and its position along the crossbar

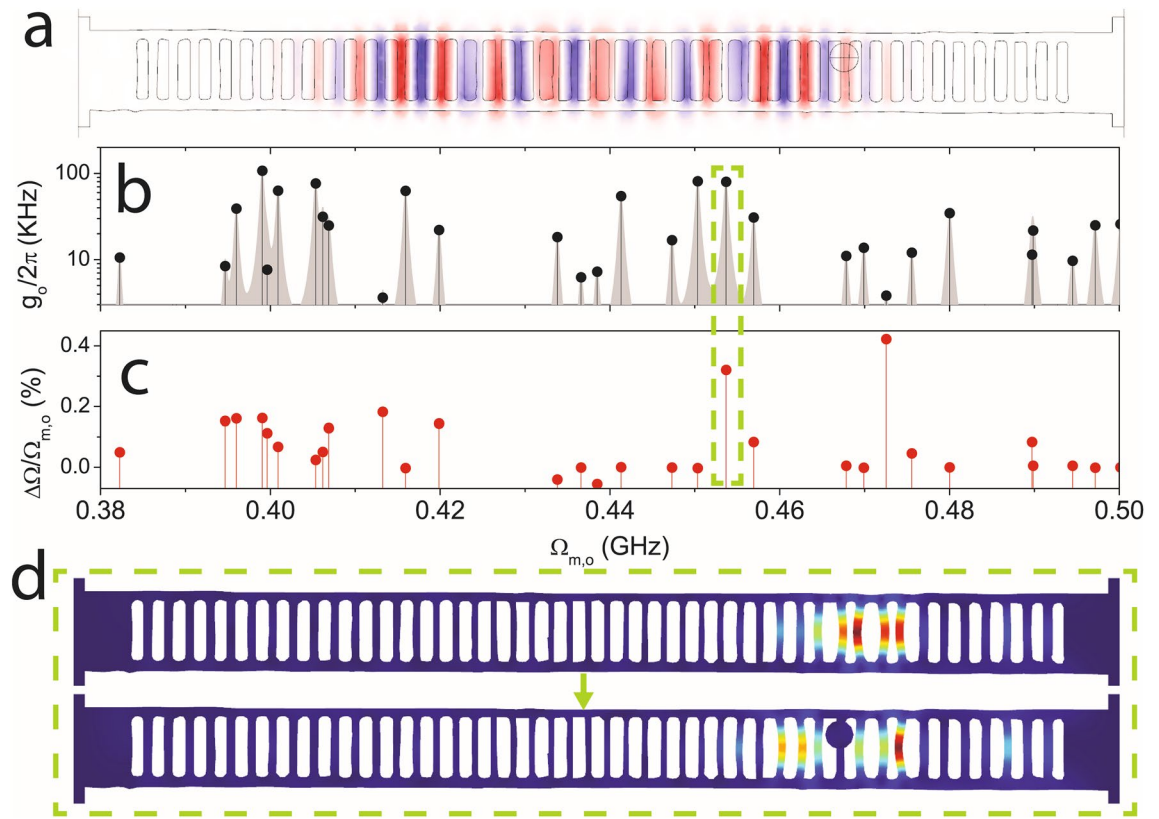


**Figure 2.** Finite-Element-Method simulations of the fabricated OMC with and without a submicrometric particle. (a) Spatial profile of the simulated optical mode employed for the evaluation of the single-particle optomechanical coupling rates ( $g_o/2\pi$ ). (b) Computed  $g_o/2\pi$  covering the frequency range of the pinch mechanical modes family. (c) Relative frequency shift of the mechanical modes with respect to the eigenfrequencies displayed by the OMC without particles. The dashed green box highlights the case of the mechanical modes visualized on panel (d). The geometry has been imported from the SEM micrograph of the fabricated OMC.

and verified that the modified mode does not change further its frequency or spatial distribution (see SI, Section S5). The previous statement holds unless there are mechanical eigenfrequencies of the isolated particle that are similar to those of the original pinch modes, in which case the modes hybridize (see SI, Section S6) similarly to what was experimentally demonstrated in Ref.<sup>19</sup> by coupling the vibrating modes of a *S. epidermidis* bacterium to those of an optomechanical disk resonator. Interestingly, the vibrating modes of that particular bacterium have an expected fundamental frequency of  $500 \pm 100$  MHz<sup>19</sup>, which is compatible with the range covered by the pinch modes of the OMC reported here. Regarding other spectral regions of interest, mechanical modes involving the deformation of the silica particle ( $d=495$  nm) start appearing at much higher frequencies (few GHz), consistent with those observed in an isolated particle of the same size (see SI, Sections S6 and S7). Another feature worth mentioning is the onset of pinch-like modes that involve the collective oscillation of the particle and the bar in contact with it (details in SI, Section S6). These latter modes appear at significantly lower frequencies than those shown in Fig. 2, given that their mass is about a factor of two larger. It is worth noting that, in Fig. 2, there is another computed mechanical mode at 0.472 GHz displaying a large frequency shift, but a very low  $g_o$  value, which would hinder its eventual RF signal.

### Experimental results

When light is coupled to the optical mode reported in Fig. 1c, thermally driven motion of the mechanical modes is seen by processing the reflected light with the spectrum analyser. Here, mechanical modes with non-negligible  $g_o$  appear as narrow Lorentzian peaks in the frequency spectrum, as reported in the bottom panel of Fig. 3. In the specific region between 0.35 and 0.55 GHz the OMC presents strong transduced signal associated to the pinch mechanical mode family. As expected, there is a rich substructure of peaks related to different cavity pinch modes coming from the same original mechanical band. Mechanical quality factors on the order of  $10^2$  are measured in this frequency region, which translate into mechanical linewidths between 1 and 3 MHz (about 0.5% of  $\Omega_{m,o}$ ). Given the frequency range of the modes and the humidity of our lab (between 45 and 50%), mechanical losses are likely dominated by viscoelastic losses due to interaction with the surrounding medium<sup>20</sup>. In fact, mechanical modes around 2 GHz presents significantly larger quality factors (see SI, section S10), which is in agreement with the inverse dependence of viscoelastic losses with frequency. The during differences between computed



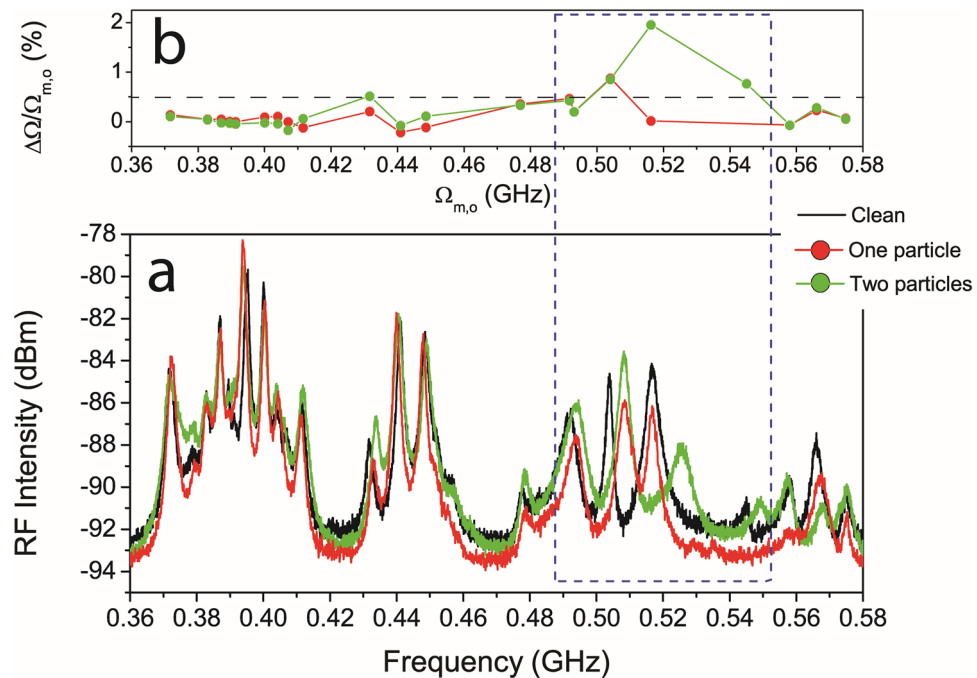


**Figure 3.** Experimental demonstration of the sensing principle (a) Transduced mechanical modes in the frequency range of the pinch modes family for the case of the as-fabricated OMC (black), the OMC with one particle (red) and with two particles (green). (b) Relative frequency shift of the mechanical modes with respect to the eigenfrequencies displayed by the as-fabricated OMC. The horizontal black dashed line corresponds to the typical mechanical linewidth of the observed modes. The blue dashed box highlights the region in which the mechanical modes are significantly affected by the presence of particles.

(Fig. 2b) and experimental (black curve of Fig. 3a)  $\Omega_{m,o}$  are probably associated to a non-negligible deviation of the sidewalls of the OMCs from verticality (see SI, Section S8), contrary to what is assumed in the simulations.

The black curve in Fig. 3a displays the mechanical spectrum of the as-fabricated OMC. When compared with the curve associated to the OMC with one particle on it (red curve), it is possible to confirm that most peaks remain relatively unaltered up to 0.48 GHz. However, above that frequency and up to about 0.55 GHz (highlighted frequency range) there is one RF peak that is strongly affected, while the others remain almost unaltered. Only a couple of the remaining RF peaks are modified as well by adding the second particle on the OMC (green curve), while the RF peaks that changed already by the inclusion of the first particle are unaffected. For instance, the RF peak appearing slightly above 0.5 GHz is only sensitive to the presence of the first particle, while the adjacent one is only sensitive to the presence of the second particle. The modified pinch modes are placed in a spectral region that would be associated to mechanical vibrations on the sides of the cavity region, which is in good agreement with the position of the particles measured by SEM as illustrated in the simulations of Fig. 2. These results demonstrate that this particular design of OMC enables the detection of single particles and the identification of the region of the resonator in which they are placed. To better illustrate the observations made on the RF spectra, in Fig. 3b we represent the frequency shift of the modes ( $\Delta\Omega$ ) with respect to the original eigenfrequency  $\Omega_{m,o}$ , for the two cases under study, i.e., one particle (red curve) and two particles (green curve). We include the mechanical linewidth limit of about 0.5% as a horizontal dashed line. This level is clearly overcome by three of the peaks under analysis within the highlighted range, demonstrating that it is relatively straightforward to detect the frequency shift caused by the presence of the particles. The obtained values exceeded those extracted from the simulations, probably because the contact region has not been accurately reproduced. In fact, it seems that from the SEM images the nanoparticles contact the OMC in more than one place, affecting two crossbars instead of only one. In any case, a qualitative good agreement with the simulations has been found. Finally, when removing the last particle, the mechanical spectrum resembles the original one, without particles, with minor relative shifts below the mechanical linewidth of the resonances (see SI, Sect. 9).

In summary, we have demonstrated the working principle of a novel sensor based on the modification, with respect to an as-fabricated reference, of the frequencies of the “pinch” mechanical modes of an optomechanical crystal cavity of the ladder type. By inspecting which of the original modes are affected, we have experimentally verified that the working principle of the sensor enables the determination of the position of submicrometer sized analytes of spherical shape along the cavity region and quantification of how many particles/analytes are deposited. These quite unique experimental and numerical observations also open the possibility of extracting a rough upper estimate of the dimensions of the analyte by inferring how many adjacent crossbars are mechanically clamped. The described technique, the accuracy of which can increase by performing a prior calibration of the OMC, reveals to be robust given that, in general, the particle blocks the contacted crossbar so that the modifications of the mechanical spectrum do not depend on the size or elastic properties of the analyte. As an

exception, FEM simulations predict that if the mechanical eigenfrequencies of the original modes and those of the analyte are brought together to the same frequency, they are expected to hybridize, so that it would be possible to also extract information about the elastic properties of the analyte and even the adhesion forces. The relatively standard fabrication requirements and large sensing response of the reported optomechanical sensor open the possibility of operating it in a fluidic environment and explore surface functionalization techniques. The latter will have new perspectives for detection of specific biological targets such as proteins, bacteria and viruses, in particular variants of COVID-19.

Received: 31 December 2020; Accepted: 26 March 2021

Published online: 09 April 2021

## References

- Nair, R. V. & Vijaya, R. Photonic crystal sensors: an overview. *Prog. Quantum Electron.* **34**(3), 89–134. <https://doi.org/10.1016/j.pquantelec.2010.01.001> (2010).
- Zhang, Y., Zhao, Y. & Lv, R. A review for optical sensors based on photonic crystal cavities. *Sens. Actuators A Phys.* **233**, 374–389. <https://doi.org/10.1016/j.sna.2015.07.025> (2015).
- Inan, H. *et al.* Photonic Crystals: emerging biosensors and their promise for point-of-care applications. *Chem. Soc. Rev.* **46**(2), 366–388. <https://doi.org/10.1039/C6CS00206D> (2017).
- Li, M., Tang, H. X. & Roukes, M. L. Ultra-sensitive NEMS-based cantilevers for sensing, scanned probe and very high-frequency applications. *Nat. Nanotechnol.* **2**(2), 114–120. <https://doi.org/10.1038/nnano.2006.208> (2007).
- Arlett, J. L., Myers, E. B. & Roukes, M. L. Comparative advantages of mechanical biosensors. *Nat. Nanotechnol.* **6**(4), 203–215. <https://doi.org/10.1038/nnano.2011.44> (2011).
- Monat, C., Domachuk, P. & Eggleton, B. J. Integrated optofluidics: a new river of light. *Nat. Photon.* **1**(2), 106–114. <https://doi.org/10.1038/nphoton.2006.96> (2007).
- Scullion, M. G., Di Falco, A. & Krauss, T. F. Slotted photonic crystal cavities with integrated microfluidics for biosensing applications. *Biosens. Bioelectron.* **27**(1), 101–105. <https://doi.org/10.1016/j.bios.2011.06.023> (2011).
- Anderson, M. J., Koehne, J. E. & Hesketh, P. J. MEMS and microfluidic devices for chemical and biosensing. *Electrochem. Soc. Interface* **28**(3), 49–53. <https://doi.org/10.1149/2.f06193if> (2019).
- Aspelmeyer, M., Kippenberg, T. J. & Marquardt, F. Cavity optomechanics. *Rev. Mod. Phys.* **86**(4), 1391–1452. <https://doi.org/10.1103/RevModPhys.86.1391> (2014).
- Gil-Santos, E. *et al.* High-frequency nano-optomechanical disk resonators in liquids. *Nat. Nanotechnol.* **10**(9), 810–816. <https://doi.org/10.1038/nnano.2015.160> (2015).
- Kippenberg, T. J., Rokhsari, H., Carmon, T., Scherer, A. & Vahala, K. J. Analysis of radiation-pressure induced mechanical oscillation of an optical microcavity. *Phys. Rev. Lett.* **95**(3), 33901. <https://doi.org/10.1103/PhysRevLett.95.033901> (2005).
- Yu, W., Jiang, W. C., Lin, Q. & Lu, T. Cavity optomechanical spring sensing of single molecules. *Nat. Commun.* **7**(1), 12311. <https://doi.org/10.1038/ncomms12311> (2016).
- Eichenfield, M., Chan, J., Camacho, R. M., Vahala, K. J. & Painter, O. Optomechanical crystals. *Nature* **462**, 78 (2009).
- Eichenfield, M., Camacho, R., Chan, J., Vahala, K. J. & Painter, O. A picogram- and nanometre-scale photonic-crystal optomechanical cavity. *Nature* **459**(7246), 550–555. <https://doi.org/10.1038/nature08061> (2009).
- Leijssen, R. & Verhagen, E. Strong optomechanical interactions in a sliced photonic crystal nanobeam. *Sci. Rep.* **5**(1), 15974. <https://doi.org/10.1038/srep15974> (2015).
- Erdil, M., Ozer, Y. & Kocaman, S. High-Q slot-mode photonic crystal nanobeam cavity biosensor with optomechanically enhanced sensitivity. *IEEE J. Sel. Top. Quantum Electron.* **25**(2), 1–6. <https://doi.org/10.1109/JSTQE.2018.2880592> (2019).
- Navarro-Urrios, D. *et al.* Optical and mechanical mode tuning in an optomechanical crystal with light-induced thermal effects. *J. Appl. Phys.* <https://doi.org/10.1063/1.4894623> (2014).
- Gomis-Bresco, J. *et al.* A One-dimensional optomechanical crystal with a complete phononic band gap. *Nat. Commun.* <https://doi.org/10.1038/ncomms5452> (2014).
- Gil-Santos, E. *et al.* Optomechanical detection of vibration modes of a single bacterium. *Nat. Nanotechnol.* **15**(6), 469–474. <https://doi.org/10.1038/s41565-020-0672-y> (2020).
- Chen, C., Ma, M., Zhe Liu, J., Zheng, Q. & Xu, Z. Viscous damping of nanobeam resonators: humidity, thermal noise, and a padding effect. *J. Appl. Phys.* **110**(3), 34320. <https://doi.org/10.1063/1.3619854> (2011).

## Acknowledgements

D. N. U. gratefully acknowledges funding from the Ministry of Science, Innovation and Universities (PGC2018-094490-B-C22) and Fundació Bosch i Gimpera (F2I-FVal\_2019-012). ICN2 is supported by the Severo Ochoa program from the Spanish Research Agency (AEI, grant no. SEV-2017-0706) by the CERCA Programme / Generalitat de Catalunya and by the Ministry of Science, Innovation and Universities (PGC2018-101743-B-I00). G. A and P.X acknowledge the support of a BIST and COFUND PREBIST studentships, respectively. E.K. and G.F. acknowledge the financial support by ERC AdG SmartPhon (Grant No. 694977).

## Author contributions

D.N.-U. and E.K. performed the experiments. D.N.-U. and G.F. devised and planned the experiments. D.N.-U., M.F.C. and N.E.C. developed the model and analysed the data. P.X., M.F.C., G.A., B.G., M.S. and C.M.S.-T. participated in the experiments at different stages. All authors contributed to the interpretation of the results and writing of the manuscript.

## Funding

Open Access funding enabled and organized by Projekt DEAL.

## Competing interests

The authors declare no competing interests.

### Additional information

**Supplementary Information** The online version contains supplementary material available at <https://doi.org/10.1038/s41598-021-87558-4>.

**Correspondence** and requests for materials should be addressed to D.N.-U. or G.F.

**Reprints and permissions information** is available at [www.nature.com/reprints](http://www.nature.com/reprints).

**Publisher's note** Springer Nature remains neutral with regard to jurisdictional claims in published maps and institutional affiliations.



**Open Access** This article is licensed under a Creative Commons Attribution 4.0 International License, which permits use, sharing, adaptation, distribution and reproduction in any medium or format, as long as you give appropriate credit to the original author(s) and the source, provide a link to the Creative Commons licence, and indicate if changes were made. The images or other third party material in this article are included in the article's Creative Commons licence, unless indicated otherwise in a credit line to the material. If material is not included in the article's Creative Commons licence and your intended use is not permitted by statutory regulation or exceeds the permitted use, you will need to obtain permission directly from the copyright holder. To view a copy of this licence, visit <http://creativecommons.org/licenses/by/4.0/>.

© The Author(s) 2021